JGR Space Physics

RESEARCH ARTICLE
10.1029/2018JA026433

Special Section:
Particle Dynamics in the Earth's Radiation Belts

Kinetic Equilibrium and Stability Analysis of Dipolarization Fronts

Alex C. Fletcher[1], Chris Crabtree[1], Gurudas Ganguli[1], David Malaspina[2], Erik Tejero[1], and Xiangning Chu[2]

[1]Plasma Physics Division, Naval Research Laboratory, Washington, DC, USA, [2]Laboratory for Atmospheric and Space Physics, University of Colorado, Boulder, CO, USA

Key Points:
- An ambipolar electric field arises due to global compression when the scale is comparable to the ion gyroradius
- This electric field leads to velocity shear that provides energy for broadband emissions
- The velocity shear-driven electron-ion hybrid instability primarily balances the compression

Correspondence to:
A. C. Fletcher,
alex.fletcher@nrl.navy.mil

Citation:
Fletcher, A. C., Crabtree, C., Ganguli, G., Malaspina, D., Tejero, E., & Chu, X. (2019). Kinetic equilibrium and stability analysis of dipolarization fronts. *Journal of Geophysical Research: Space Physics*, *124*, 2010–2028. https://doi.org/10.1029/2018JA026433

Received 21 DEC 2018
Accepted 4 MAR 2019
Accepted article online 9 MAR 2019
Published online 30 MAR 2019

Abstract Dipolarization fronts are typically observed with a density gradient of scale size comparable to an ion gyroradius, which naturally results in an ambipolar electric field in the direction of the gradient. Prevailing models ignore this ambipolar electric field, the separation of ion and electron scale physics, and consequent non-Maxwellian plasma distributions with strong spatial gradients in velocity, all of which we investigate in this paper. We examine two dipolarization front events observed by the Magnetospheric Multiscale mission (one with low plasma beta, one with high plasma beta), develop a rigorous kinetic equilibrium for dipolarization fronts, analyze the linear stability, and explore the nonlinear evolution and observable signatures with kinetic simulations. There are two major drivers of instability in the lower-hybrid frequency range: the density gradient (lower-hybrid drift instability) and the velocity shear (electron-ion hybrid instability). We argue the electron-ion hybrid mode is dominant, and consequently a dipolarization front approaches a steady or saturated state through the emission of waves that relax the velocity shear. A key aspect of these shear-driven waves is a broadband frequency spectrum that is consistent with satellite observation.

1. Introduction

Dipolarization fronts (DFs) are observationally characterized by a rapid rise in the northward component of the magnetic field, a large Earthward flow velocity, a sharp drop in the plasma density, and the onset of broadband wave activity. These changes in plasma parameters are due to a flux tube rapidly propagating past the observing spacecraft. DFs are often observed during bursty bulk flow events (Runov et al., 2009), during which large-scale magnetic flux tubes that have been depleted of plasma (Sergeev et al., 1996) by some event (likely transient reconnection; Sitnov et al., 2009) propagate rapidly toward the Earth to equalize the quantity $pV^{5/3}$, where p is the plasma thermal pressure and V is the flux tube volume (C. X. Chen & Wolf, 1993). Flux tubes that have been depleted more than neighboring flux tubes will have a larger Earthward velocity, leading to a compression of the plasma at the edge as the faster moving flux tube overtakes the slower moving flux tube. This compression maintains the plasma gradients as the flux tube propagates Earthward and must be balanced by some physical mechanism. In this paper we develop a kinetic equilibrium solution to the Vlasov-Maxwell system and argue that the mesoscopic compression leads to quasistatic structures with scale sizes comparable to or less than the ion gyroradius with strong velocity gradients, which is unstable to the generation of broadband waves in the lower-hybrid frequency range. The waves act on the plasma to limit the compression.

Dispersionless injections inside of geosynchronous orbit are not uncommon (Nosé et al., 2010; Reeves et al., 1996), though they were infrequently reported in the literature (Nosé et al., 2010). However, since the Van Allen probe era, renewed attention (Gkioulidou et al., 2014, 2015, J. Liu et al., 2016) has been placed on injections and DFs that continue into the radiation belts where they can impact energetic particle populations. Both the quasistatic electromagnetic fields (Sorathia et al., 2018) and the waves that are associated with the DF (Hwang et al., 2014) have been shown to be important for energizing particles at a DF. The properties of DFs are different in the inner magnetosphere than in the magnetotail (Ukhorskiy et al., 2017) and thus it is important to develop a self-consistent model of DFs to understand the kinetic scale structure of DFs and the waves that must accompany them in order to accurately assess the particle acceleration in both the inner and outer magnetospheres.

Satellite observations indicate that the plasma in a DF is compressed across the magnetic field to scale sizes comparable to the ion gyroradius (Runov et al., 2009; which is of the same order as the ion inertial length when the plasma $\beta_i = 8\pi p_i/B^2 \sim 1$, i.e., the ion thermal energy density p_i is comparable to the magnetic field energy density $B^2/(8\pi)$). This compression is accompanied by broadband wave activity at observed frequencies around the local lower-hybrid frequency, which dissipates the compression. Recently, C. M. Liu et al. (2018) have presented Magnetospheric Multiscale (MMS) measurements of an electron jet and a persistent normal electric field within a DF.

DF dynamics have generally been analyzed through global simulations (e.g., Birn et al., 2011; Birn & Hesse, 2014; Sitnov et al., 2014; Wan & Lapenta, 2008). Because the scale sizes are of the order of an ion gyroradius or less, kinetic effects become important and fluid models are inadequate. Global scale kinetic simulations that are capable of resolving a DF are still not practical because they use artificially low mass ratios and insufficient particles per cell to accurately resolve gyro scales for ambipolar effects. Our kinetic analysis shows that the ambipolar effects are critical for the local dynamics in DFs, which then determine energy dissipation. So we adopt a complementary path to study the small dissipation scale physics of a DF by using kinetic analysis locally in the DF frame. In addition, we anchor our theory to reality by ensuring that our distribution function reproduces the distinguishing character of the observed density and magnetic field profiles. Consequently, our results may be used to validate global kinetic simulations when they approach gyro scales.

Many wave modes have been proposed to accompany a DF in both the magnetotail and the inner magnetosphere, including broadband lower-hybrid drift (LHD) waves (Zhou et al., 2009), electrostatic solitary waves (Malaspina et al., 2014), and kinetic Alfvén waves (Chaston et al., 2014). In this work, we focus on the broadband (mostly electrostatic) emissions that are observed coincident with the density drop at the Earthward edge of the DF and develop theory and simulation to show how such waves naturally arise from a shear flow instability at the front. Since the scale size of the DF in this region is of the order of the ion gyroradius, any theory of these waves must take into account the strong background inhomogeneities.

In section 2 we describe two cases of DFs as measured by the MMS spacecraft, one with low beta and the other with high beta, that motivate the subsequent analysis. In section 3 we extend the equilibrium from Ganguli et al. (2018) to be electromagnetic and include temperature gradients and temperature anisotropy. In section 4 we use the resulting plasma distribution function to study the linear stability of the equilibrium by developing the appropriate eigenvalue condition and show that sheared flow-driven modes are naturally generated in a typical DF. In section 5 we study the nonlinear evolution using a particle-in-cell (PIC) simulation and show that the velocity shear-driven waves can relax the gradients and lead to a steady or saturated state consistent with a broadband spectral signature similar to satellite observations. In section 6 we discuss the consequences of our results.

2. MMS Measurements

Here we describe specific DF measurements from the MMS satellites (Burch et al., 2016). The components of the magnetic field are measured by a fluxgate magnetometer (Russell et al., 2016). The densities are obtained from the Fast Plasma Investigation (Pollock et al., 2016) and the Energetic Ion Spectrometer (Mauk et al., 2016). FIELDS data (Torbert et al., 2016) are used to determine both the flow ($\vec{E} = -\vec{u} \times \vec{B}$) and the power spectral density of the waves.

The first examined event, which we refer to as low beta case, occurred at approximately 13:56:59 UTC on 16 May 2017. We find the average normal direction (in GSE coordinates) to be $\hat{n} = (0.73, -0.17, 0.66)$. This event occurred approximately −14.5 Earth radii down-tail and passed the spacecraft at 225 ± 8 km/s. Plasma beta ($\beta_e = 8\pi n \kappa T_e/B^2$) is ∼0.58, which is consistent with weak compression. This was the event analyzed in Ganguli et al. (2018). An overview of this event is shown in Figure 1. Magnetic dipolarization is apparent between the dashed lines of Figure 1b and the associated drop in plasma density is seen in Figure 1d. Figure 1g shows the characteristic broadband wave emission (Malaspina et al., 2015).

The second examined event, which we refer to as the high beta case, occurred at approximately 21:24:44 UTC on 8 June 2017. We find the average normal direction (in GSE coordinates) to be $\hat{n} = (0.72, -0.58, 0.38)$,

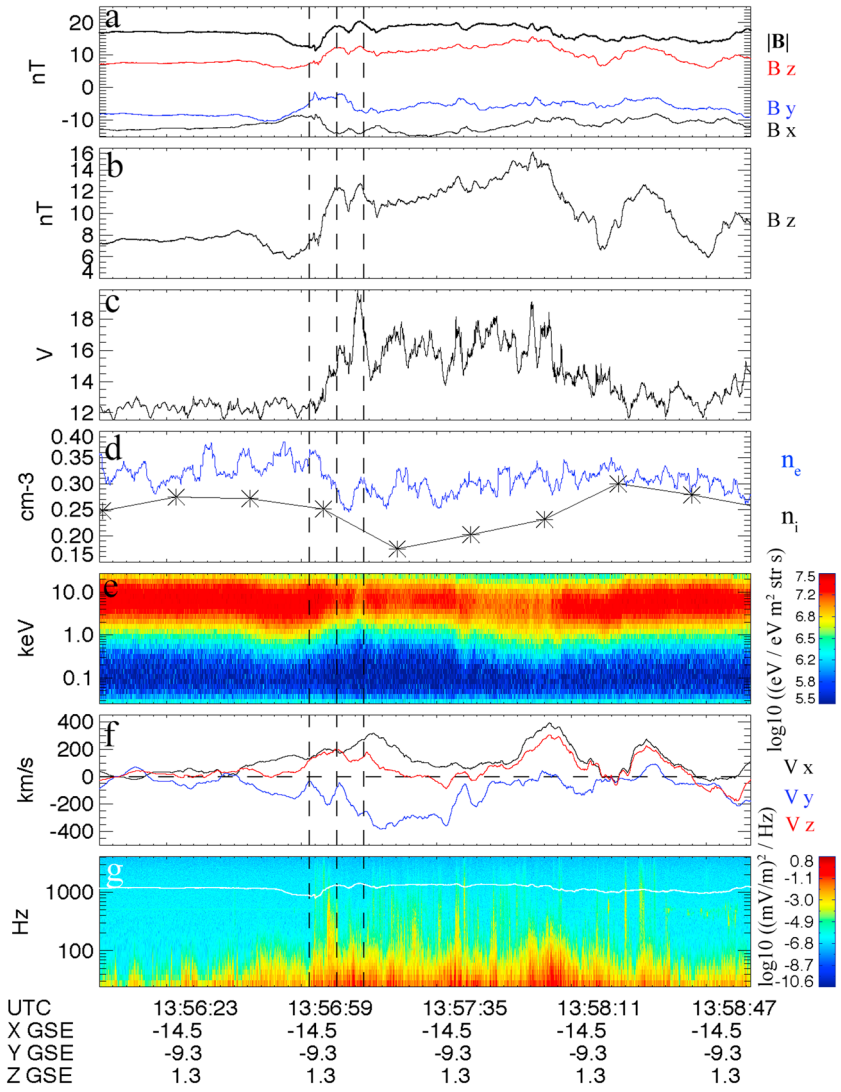

Figure 1. Magnetospheric Multiscale fields and particle data during a weak compression dipolarization front. (a and b) Low-frequency magnetic field data. (c) Spacecraft floating potential. (d) Electron and proton density. (e) Electron omni-directional energy flux. (f) Plasma flow velocity components. (g) Electric field wave power spectral density (the white line is the local electron cyclotron frequency).

where the analysis from each spacecraft agrees to within 0.5°. β_e is ~15 for this case. An overview of this event is shown in Figure 2. The front passed the spacecraft at 211 ± 10 km/s.

To analyze the data using our equilibrium model in section 3 and stability analysis in section 4, we need to convert time to space by estimating the propagation of the front and assuming that the slow scale variations (not the high frequency waves) are due to the propagation of the front. To do this we use data from all four spacecraft. We first use a minimum variance analysis with the magnetic time series data to estimate the normal direction to the front. Then we shift the time series from each spacecraft to minimize the difference between the time series. With this timing information, the direction of the normal to the front, and the spacecraft locations we can estimate the velocity of the front. The mean estimate of velocities from each spacecraft lies within the estimated error bar of the velocity estimate from each pair of spacecraft. Figure 3 shows an example of this velocity estimate for the high beta case.

With this velocity estimate and an estimate of temperature and magnetic field upstream of the layer, we convert time to space normalized to the reference ion gyroradius. We then rotate the three components of the magnetic field so that the transformed $\hat{e}_z$ coordinate captures the maximum variation (in the $\hat{e}_x$ direction) of the magnetic field (corresponding to the field produced by the local current).

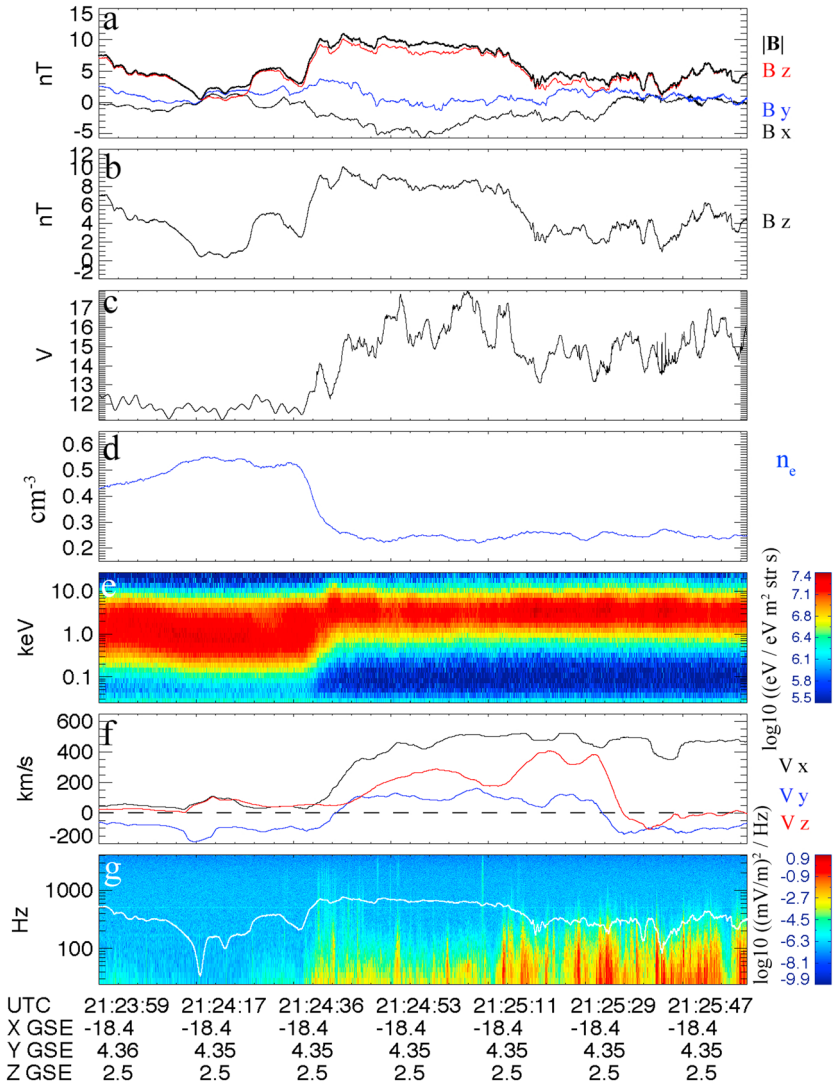

Figure 2. Magnetospheric Multiscale fields and particle data during a strong compression dipolarization front. (a and b) Low-frequency magnetic field data. (c) Spacecraft floating potential. (d) Electron and proton density. (e) Electron omni-directional energy flux. (f) Plasma flow velocity components. (g) Electric field wave power spectral density (the white line is the local electron cyclotron frequency).

3. Kinetic Equilibrium

In order to model the two cases discussed in section 2, we develop a kinetic equilibrium that is a solution to the Vlasov-Maxwell system of equations in the time stationary limit, that is,

$$\begin{aligned} \vec{v}\cdot\nabla_{\vec{x}} f_s + \frac{q_s}{m_s}\left(\vec{E}+\frac{\vec{v}}{c}\times\vec{B}\right)\cdot\frac{\partial}{\partial\vec{v}} f_s(\vec{x},\vec{v}) = 0 \\ \nabla\cdot\vec{E} = \sum_s 4\pi q_s \int d^3\vec{v} f_s \\ \nabla\times\vec{B} = \frac{4\pi}{c}\sum_s \int d^3\vec{v} q_s \vec{v} f_s. \end{aligned} \tag{1}$$

In the DF frame the variation in the normal direction (with scale size of an ion gyroradius) is orders of magnitude stronger than in the orthogonal directions. Hence, for small dissipation scale physics it becomes essentially a one-dimensional model. The local magnetic field is in the $\vec{e}_z$ direction and varies in the $\vec{e}_x$ direction, that is, $\vec{B} = B(x)\vec{e}_z$, while a nonuniform electrostatic potential also varies in the $\vec{e}_x$ direction, that is, $\phi(x)$. We introduce a vector potential, $\vec{A}$, where $\vec{B} = \nabla\times\vec{A}$ and $\vec{A} = A(x)\vec{e}_y$. The Hamiltonian is

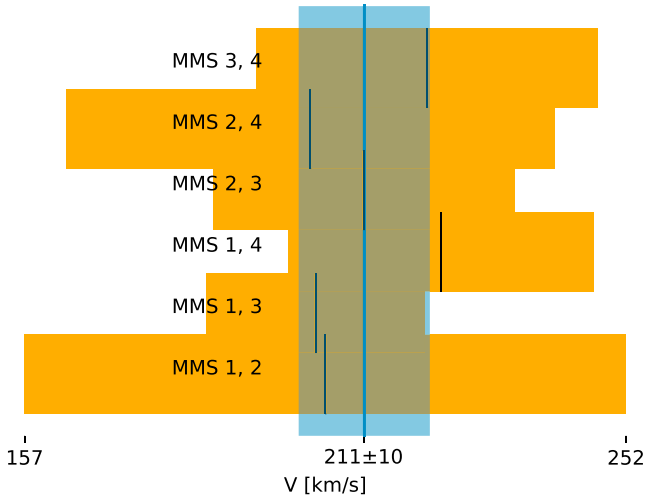

Figure 3. Estimate of the velocity of the dipolarization front passing the four MMS spacecraft for the high beta case. MMS = Magnetospheric Multiscale.

$$H_\alpha(x) = \frac{p_x^2}{2m_\alpha} + \frac{1}{2m_\alpha}\left[p_y - \frac{q_\alpha}{c}A(x)\right]^2 + \frac{p_z^2}{2m_\alpha} + q_\alpha\phi(x), \tag{2}$$

where α is the species; m_α is the mass; q_α is the charge; and p_x, p_y, and p_z are the canonical momenta. The Hamiltonian only depends on x and is independent of t, y, and z, so H, p_y, and p_z are constants of motion, where $p_y = m_\alpha v_y + m_\alpha\Omega_\alpha a(x)$. Since the constants are in involution, the dynamics is completely integrable. The cyclotron frequency is Ω_α, $a(x) = A(x)/B_0$, and B_0 is the upstream background magnetic field. It follows that the guiding center position,

$$x_{g\alpha}(a) = \frac{p_y}{m_\alpha\Omega_\alpha} = a(x) + \frac{v_y}{\Omega_\alpha}, \tag{3}$$

is a constant of motion as well.

3.1. Distribution Function

A distribution function that is a function of the constants of motion satisfies the Vlasov equation (Nicholson, 1983). Thus, we may construct a rigorous solution to the Vlasov equation that is Maxwellian away from the front but accounts for a density gradient across the front as follows:

$$f_{0\alpha}(x,\vec{v}) = \frac{N_{0\alpha}}{\left(\pi v_{t\alpha}^2\right)^{3/2}} Q_\alpha(x_{g\alpha}) \exp\left(-\frac{E_\alpha(x)}{\kappa T_\alpha}\right), \tag{4}$$

where the energy, $E_\alpha = m_\alpha v^2/2 + q_\alpha\phi(x)$, is also a constant of motion, $v_{t\alpha} = \sqrt{2\kappa T_\alpha/m_\alpha}$ is the thermal velocity, κ is the Boltzmann constant, $N_{0\alpha}$ is the plasma density upstream of the layer, and Q_α is the distribution of guiding centers that produces the gradient. The distribution of guiding centers is given by

$$Q_\alpha(x_{g\alpha}) = \begin{cases} R_\alpha & x_{g\alpha} < x_{g1\alpha} \\ R_\alpha + (S_\alpha - R_\alpha)\left(\frac{x_{g\alpha}-x_{g1\alpha}}{x_{g2\alpha}-x_{g1\alpha}}\right) & x_{g1\alpha} < x_{g\alpha} < x_{g2\alpha} \\ S_\alpha & x_{g\alpha} > x_{g2\alpha} \end{cases}. \tag{5}$$

The density jump is $N_{0\alpha}(R_\alpha - S_\alpha)$ over a distance of $x_{g2\alpha} - x_{g1\alpha}$. The parameters R_α, S_α, $x_{g1\alpha}$, and $x_{g2\alpha}$ are model inputs determined from observations. The separation of ion and electron scale physics can be provided by different values of the parameters $x_{g1\alpha}$ and $x_{g2\alpha}$ for each species (electrons and protons). This separation is necessary to reproduce the observed density and magnetic field profiles. In the following subsection we compute the moments of this distribution function analytically. The first two of moments are needed to calculate the sources in Maxwell's equations in equation (1). This allows us to identify the physical attributes of the observed DF exactly. The choice of these model parameters particularizes the distribution function to a given DF.

3.2. Moments

The moments of the distribution provide the physical attributes of the equilibrium configuration, in particular their spatial variations. The zeroth moment (density) is

$$n_\alpha(a) \equiv \langle f_{0\alpha} \rangle = \int f_{0\alpha}(\vec{v}, \phi(a))\, d\vec{v} = N_{0\alpha} \frac{(R_\alpha + S_\alpha)}{2} \exp\left(-\frac{q_\alpha \phi(a)}{\kappa T_\alpha}\right) Y_\alpha(a) \tag{6}$$

with

$$Y_\alpha(a) = 1 \pm \left(\frac{R_\alpha - S_\alpha}{R_\alpha + S_\alpha}\right)\left(\frac{1}{\zeta_{1\alpha} - \zeta_{2\alpha}}\right) \times \left\{ \zeta_{2\alpha}\mathrm{erf}(\zeta_{2\alpha}) - \zeta_{1\alpha}\mathrm{erf}(\zeta_{1\alpha}) + \frac{1}{\sqrt{\pi}}\left[\exp(-\zeta_{2\alpha}^2) - \exp(-\zeta_{1\alpha}^2)\right] \right\}. \tag{7}$$

The error function is erf, $\zeta_{\alpha 1,2} = \Omega_\alpha(a(x) - x_{g\alpha 1,2})/v_{t\alpha}$, and $\pm$ refers to the species charge. Here we note the dependence of various quantities on $a(x)$ in equations (6) and (7), instead of just x; $a(x)$ will be determined from the first moment (i.e., the current density). The electrostatic potential is found via quasineutrality, $n_e \approx n_i$, which is equivalent to solving Poisson's equation in the limit that the Debye length is much smaller than the scale length of the plasma:

$$\phi(a) = \frac{\kappa^2 T_e T_i}{q_e \kappa T_i - q_i \kappa T_e} \ln\left[\frac{N_{0e}(R_e + S_e)Y_e}{N_{0i}(R_i + S_i)Y_i}\right]. \tag{8}$$

Because ∇n, ∇B, and the electric field, $\vec{E}(a) = \nabla\phi(a)$, are in the $\vec{e}_x$ direction, and the magnetic field is in the $\vec{e}_z$ direction, the only nonzero component of the flow is in the $\vec{e}_y$ direction. The flow is

$$\begin{aligned} u_{y\alpha}(a) &\equiv \left\langle v_y f_{0\alpha} \right\rangle / n_\alpha = \frac{1}{n_\alpha} \int v_y f_{0\alpha}(\vec{v}, \phi(a))\, d\vec{v} \\ &= \pm \frac{\exp\left(\frac{-2q_\alpha\phi(a)}{m_\alpha v_{t\alpha}^2}\right) N_{0\alpha}(R_\alpha - S_\alpha) v_{t\alpha}[\mathrm{erf}(\zeta_{2\alpha}) - \mathrm{erf}(\zeta_{1\alpha})]}{4 n_\alpha(\zeta_{1\alpha} - \zeta_{2\alpha})} \end{aligned} \tag{9}$$

and includes the diamagnetic drift, grad-B drift, and $\vec{E} \times \vec{B}$ drift.

The magnetic field produced by the current density inherent in the equilibrium distribution function is found via

$$\frac{dB_z}{dx} = -\frac{4\pi}{c} j_y, \tag{10}$$

where $j_y = \sum_\alpha q_\alpha n_\alpha u_{y\alpha}$ is the current density. With B_z, the vector potential is found via

$$\frac{da}{dx} = \frac{B_z}{B_0} \tag{11}$$

with appropriate initial conditions. Equations (10) and (11) do not have a readily apparent closed-form solution but can be integrated numerically quite easily. The current density in Ampere's law can be written explicitly as a function of the vector potential $a(x)$. Thus, we can numerically solve equations (10) and (11) for the function $a(x)$ which then provides a mapping to x. All plasma parameters that have been determined as a function of a can now be found as a function of x. An electrostatic approximation is equivalent to specifying $a(x)$ explicitly (e.g., for a uniform magnetic field, $a(x) = x$).

We can continue and consider higher order moments. For the pressure tensor, integrals over v_x and v_z are zero, meaning all off diagonal terms vanish and

$$p_{\alpha xx} = p_{\alpha zz} = n_\alpha \kappa T_\alpha. \tag{12}$$

The remaining component is

$$p_{\alpha yy}(a) = n_\alpha \kappa T_\alpha \left[1 \pm \frac{\exp\left(\frac{-2q_\alpha\phi(a)}{m_\alpha v_{t\alpha}^2}\right)\left(e^{-\zeta_{2\alpha}^2} - e^{-\zeta_{1\alpha}^2}\right) N_{0\alpha}(R_\alpha - S_\alpha)}{2 n_\alpha \sqrt{\pi}(\zeta_{1\alpha} - \zeta_{2\alpha})}\right]. \tag{13}$$

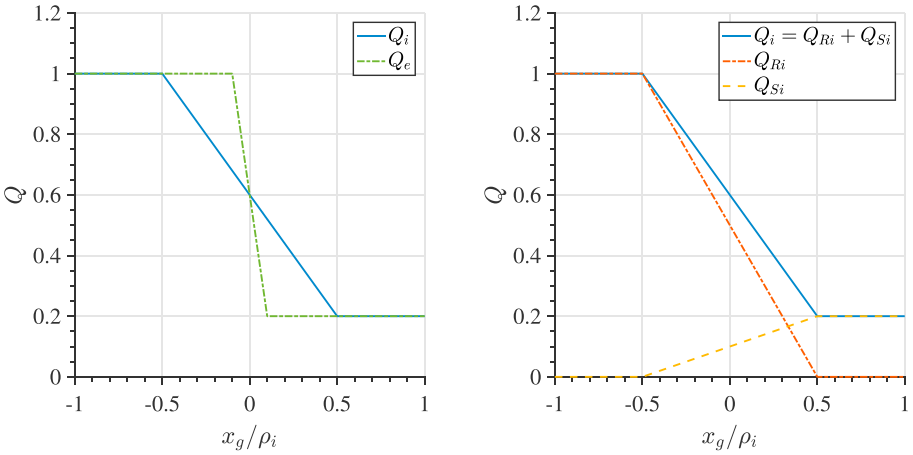

Figure 4. The distribution of guiding centers for ions and electrons (left) and the distribution of guiding centers for the ions with a temperature gradient (right).

3.3. Temperature Gradient and Anisotropy

Ganguli et al. (2018) found that this distribution function fits lower β MMS cases well in the electrostatic limit. In these cases, the temperature gradient and anisotropy are small and can be neglected. However, this is a limiting case and normally DFs display both temperature gradients and anisotropy. We derive a more general distribution function including temperature gradient and anisotropy by considering separately the plasma on the higher density side, denoted by the subscript R (with temperatures $T_{\alpha,R\perp}$ and $T_{\alpha,R\parallel}$), and on the lower density side, denoted by the subscript S (with temperatures $T_{\alpha,S\perp}$ and $T_{\alpha,S\parallel}$). The corresponding distribution function is

$$f_{0\alpha}(x,\vec{v}) = \frac{N_{0\alpha}}{\pi v_{t\alpha,R\perp}^2\sqrt{\pi v_{t\alpha,R\parallel}^2}} Q_{R\alpha}(x_{g\alpha}) \exp\left(-\frac{v_x^2+v_y^2}{v_{t\alpha,R\perp}^2} - \frac{v_z^2}{v_{t\alpha,R\parallel}^2} - \frac{q_\alpha\phi(x)}{\kappa T_{\alpha,R\perp}}\right) + \frac{N_{0\alpha}}{\pi v_{t\alpha,S\perp}^2\sqrt{\pi v_{t\alpha,S\parallel}^2}} Q_{S\alpha}(x_{g\alpha}) \exp\left(-\frac{v_x^2+v_y^2}{v_{t\alpha,S\perp}^2} - \frac{v_z^2}{v_{t\alpha,S\parallel}^2} - \frac{q_\alpha\phi(x)}{\kappa T_{\alpha,S\perp}}\right). \quad (14)$$

The gradient in the electrostatic potential is entirely in the direction perpendicular to the magnetic field, so it is the perpendicular temperature that appears in the denominator of the ϕ term in equation (14). $Q_{R\alpha}$ is found by setting $S_\alpha = 0$ in equation (5) while $Q_{S\alpha}$ is found by setting $R_\alpha = 0$ in equation (5). Figure 4 shows the distribution of guiding centers. Note that while these functions are not smooth, the physical attributes of the plasma (i.e., the moments found above) are still smooth due to velocity averaging.

We do not allow different layer widths for the density and temperature profiles, for example, $x_{g1\alpha,R} = x_{g1\alpha,S} = x_{g1\alpha}$ and $x_{g2\alpha,R} = x_{g2\alpha,S} = x_{g2\alpha}$, though estimating separate temperatures on each side of the layer is now necessary. The parameter $\zeta_{\alpha1,2} = \Omega_\alpha(x - x_{g\alpha1,2})/v_{t\alpha\perp}$ is now defined with the perpendicular temperature. All moments follow in the same way as before.

3.4. Application to MMS Data

We now compare the equilibrium derived in sections 3.1 and 3.2 to the MMS data. In order to do this, we calculate the moments (equations (6), (9), and (13)) and magnetic field (equation (10)). The necessary boundary condition parameters (R_α, S_α, $T_{\alpha,R\perp}$, $T_{\alpha,S\perp}$, $T_{\alpha,R\parallel}$, $T_{\alpha,S\parallel}$, and B_0) and model parameters ($x_{g\alpha1,2}$) are determined with a fitting procedure. The fit minimizes the error between the theoretical and observed density, temperature, and magnetic field simultaneously by altering these aforementioned boundary condition parameters and model parameters. A simplex search method in MATLAB is used for the fitting. For a layer in which the density is well resolved (e.g., the low beta case), only the guiding center parameters, $x_{g\alpha1,2}$, must change to reproduce the measurements (whereas the boundary conditions are found from averaging data upstream and downstream of the layer). In a marginally resolved layer (e.g., the high beta case), it is necessary to fit all parameters in order to match the observed density, temperature, and magnetic field simultaneously. This procedure is similar to enforcing boundary conditions to particularize the solution to

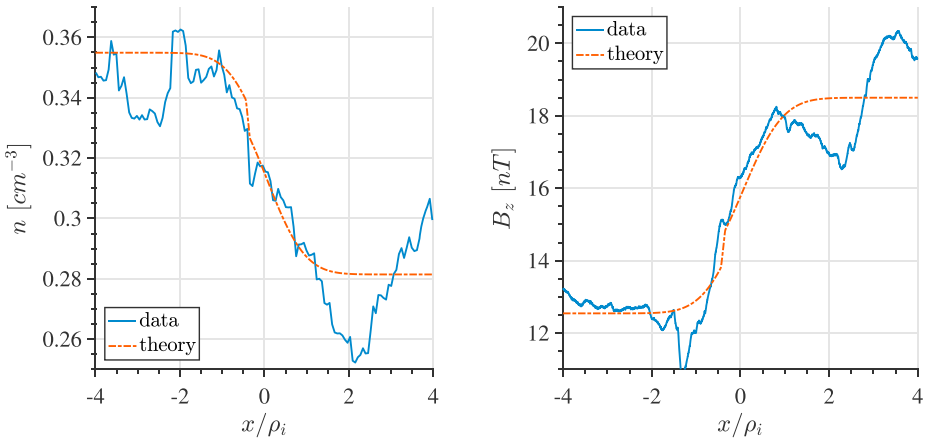

Figure 5. The plasma density (left) and magnetic field (right) for the low beta from Magnetospheric Multiscale and the model that best fits these data.

a specific DF. We obtain the boundary conditions from observations in order to anchor our model to reality, but alternatively it may be obtained from the output of a global model if the model can resolve the smaller scale sizes with sufficient accuracy.

3.4.1. Low Beta Case

The low beta case is best fit by the parameters $R = 1.00, S = 0.793, x_{g1e} = -0.438\rho_i, x_{g2e} = -0.346\rho_i, x_{g1i} = -0.0390\rho_i, x_{g2i} = 0.850\rho_i, n_0 = 0.355$ cm^{-3}, $\kappa T_{e0} = 654.62$ eV, $T_i/T_e = 6.714$, and $B_0 = 12.55$ nT, where $\rho_i = \frac{mcv_\perp}{|q|B_0}$ is the ion gyroradius. Note that $R_i = R_e$ and $S_e = S_i$ and that the low beta case has no temperature anisotropy (i.e., $T_{\alpha\perp} = T_{\alpha\parallel}$). Figure 5 shows the plasma density and magnetic field for the MMS low beta event and the theory. We use MMS 2, but the results do not change significantly if another satellite is used. The temperature is approximately constant across the layer and there is no need for the temperature gradient formulation of the distribution function (equation (14)). The electrostatic approximation ($a(x) = x$) is sufficient for this case because of the lower beta ($\beta_e \approx 0.58$). Note that, under the electrostatic approximation, the magnetic field is not self consistent and merely calculated after the fact from j_y.

Of note is the presence of a smaller "layer within a layer" on the electron scale located at $x/\rho_i \approx -0.4$. The width of this electron layer is greater than an electron gyroradius but less than an ion gyroradius, effectively making the ions unmagnetized within it. The electron layer's location cannot be determined with certainty from the data simply because the DF is passing by the spacecraft too quickly (over 200 km/s). However, the existence of an electron layer of this approximate scale size can be inferred via the total change in the magnetic field across the layer. For layer widths much larger than the determined width the ions would

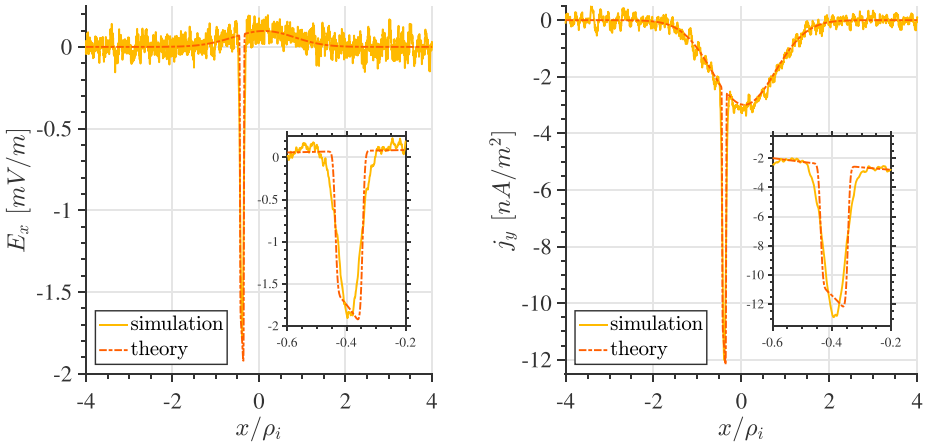

Figure 6. The electric field (left) and current density (right) for the low beta case from Magnetospheric Multiscale and particle-in-cell simulation of the associated model. The insets show the spike around the electron scale layer.

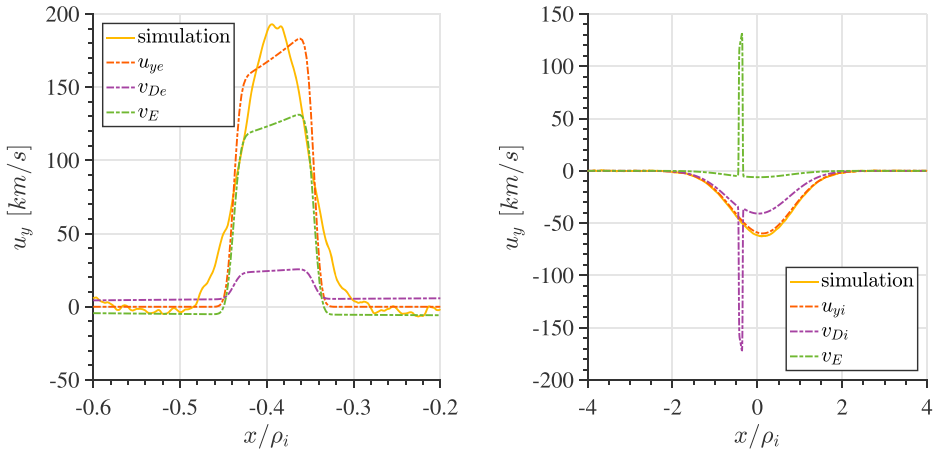

Figure 7. The flow from the particle-in-cell simulation compared to the modeled flow for electrons (left) and ions (right). The component modeled drifts are also shown; the $\vec{E}\times\vec{B}$ drift dominates for the electrons and the diamagnetic drift dominates for the ions. Note that the spatial scale on the left is much smaller than the rest of the figures in order to show the electron layer.

experience a full $\vec{E}\times\vec{B}$ drift velocity, rather than a reduced drift velocity, such that the ions would drift with the electrons and not lead to enough current flowing in the layer to explain the observed change in the magnetic field. The fit matches the jumps in density and magnetic field well overall, though in both this case and the following one there are oscillations that could possibly be a wave that would not be captured by the equilibrium model.

3.4.2. Equilibrium Simulation

To verify the low beta equilibrium, we perform an electrostatic PIC simulation initialized to the distribution function (equation (4)) and background parameters. Like the equilibrium, this simulation is one dimensional. If a second or third dimension are included, instabilities can occur; this is the topic of sections 4 and 5. The PIC code is mostly standard (Birdsall & Langdon, 2004) and uses a high-order volume preserving particle pusher (He et al., 2015), a high-order finite difference solution to Poisson's equation (Sutmann, 2007), and cubic splines for interpolation.

Two mirrored layers are generated at $\pm x_0$ with periodic boundary conditions. The separation of the layers is $20\rho_i$. We verify that the equilibrium is stable and that no transients exist over several ion gyroperiods, and then average to reduce noise and thus enable comparison to theory. The number of cells is 50,000 (where each cell is $\sim\lambda_D$, the Debye length) and the number of particles is 268 million.

Figure 6 shows the electric field and current for both the simulation and the model. Additionally, the density and magnetic field in the simulation match well with the theory curves in Figure 5. The density and flow are apparent without averaging (not shown), but the electric field is below the noise of the simulation and has the expected shape only on average, where averaging is performed in both time and space. The electron layer at $x/\rho_i \approx -0.4$ is more apparent in Figure 6, particularly the significantly larger electric field within the electron layer.

3.4.3. Kinetic Versus Fluid Models

While Figure 6 contains the current density, it is worth discussing the flow, u_y, of each species and the drifts that make up that flow as well. Figure 7 shows the flow of electrons and ions separately, along with $\vec{E}\times\vec{B}$ drift, $\vec{v}_E = c\vec{E}\times\vec{B}/B^2$, and the diamagnetic drift, $\vec{v}_{D\alpha} = \mp\nabla P_\alpha \times \vec{B}/(enB^2)$. B is uniform here so the grad-B drift is absent. The electron's diamagnetic and $\vec{E}\times\vec{B}$ drifts are in the same direction within the smaller electron layer, and are zero outside of it. The electron diamagnetic drift is an order of magnitude smaller than the $\vec{E}\times\vec{B}$ drift. This is consistent with observations of electron jets (C. M. Liu et al. 2018). The ions, on the other hand, have diamagnetic and $\vec{E}\times\vec{B}$ drifts that add within the ion layer but cancel each other out within the electron layer. The net result is that the ion flow does not change within the electron layer, and ions effectively do not "see" the electric field at its peak value in the electron layer, mainly due to the renormalization of the gyrofrequency by velocity shear as explained in Ganguli et al. (2018). These differences in the ion and electron drifts define the ion and electron layers and are important for the stability

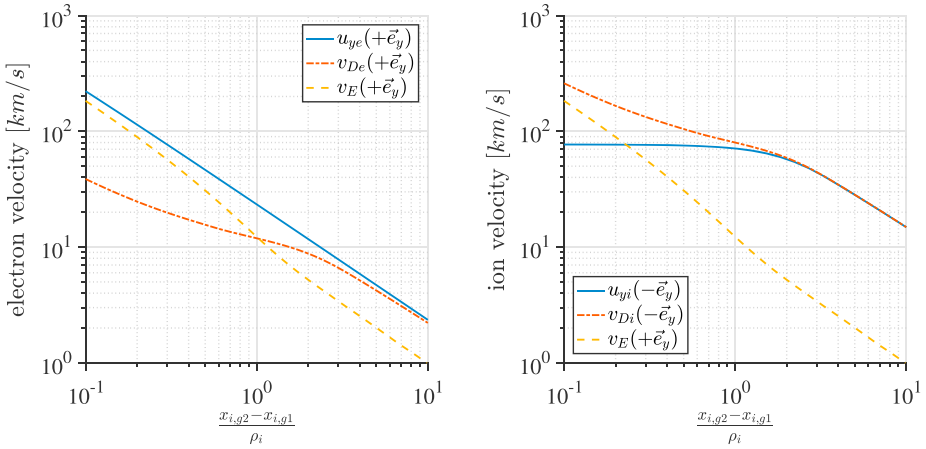

Figure 8. The maximum flow within the electron layer for electrons (left) and ions (right), along with the component drifts, as a function of dipolarization front layer width. Note the dominance of the $\vec{E}\times\vec{B}$ for the electrons for small dipolarization front layer widths.

analysis in section 4. Separate ion and electron layers were observed in the compressed plasma layer in the plasma sheet/lobe interface (Parks et al., 1979).

The difference between the two species' drifts is more apparent in Figure 8, which shows the maximum amplitude of each drift and the flow within the layer as a function of layer width. The parameters here are the same for the low beta case described above, except $x_{g\alpha 1,2}$ vary to create different layer widths. For layer widths greater than an ion gyroradius, the diamagnetic drift dominates for both species. However, for layer widths smaller than an ion gyroradius, the $\vec{E}\times\vec{B}$ drift dominates for the electrons. For the ions the flow approaches an asymptote as the layer width decreases. This is a key difference between the kinetic and fluid approaches to modeling DFs. The implications of this difference will also be discussed further in the stability analysis of section 4.

Another kinetic effect is the saturation of the magnitude of the electric field, which is shown as a function of layer width in Figure 9. In the fluid picture, $\vec{E}\propto\nabla P$, and the electric field would instead become singular as the layer width gets smaller.

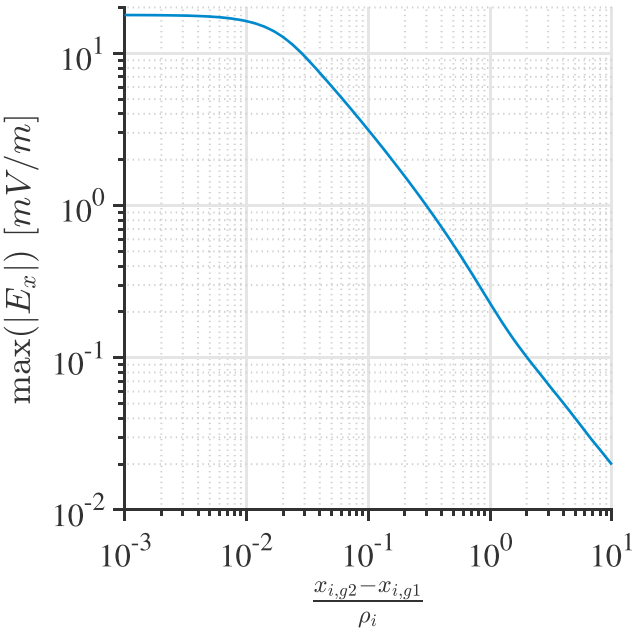

Figure 9. The maximum electric field within the electron layer as a function of layer width. The saturation is a kinetic effect that is not present in a fluid model.

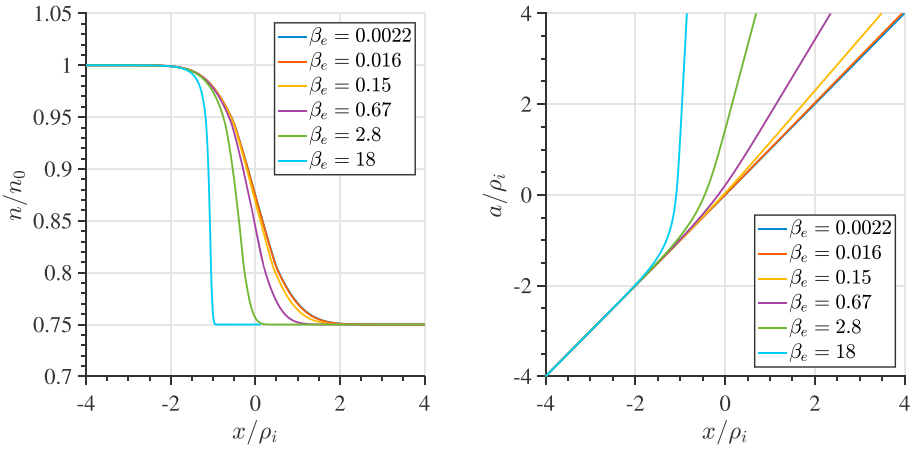

Figure 10. The plasma density (left) and vector potential (right) for six different beta values.

3.4.4. Electromagnetic Effects

The relative importance of electromagnetic effects can be seen in Figure 10, which was constructed with a similar layer width to the low beta case above but with varying temperatures and magnetic fields to produce different values of beta. The electrostatic approximation corresponds to $a(x) = x$, that is, a diagonal line in the right plot of Figure 10. As β_e increases, the shape of $a(x)$ deviates. Since the moments, fields, and potentials were all determined as functions of a, after which $a(x)$ was determined, $a(x)$ is simply a mapping that condenses the DF in the $\hat{e}_x$ direction. This is seen in the density on the left of Figure 10. The electrostatic approximation is very good for $\beta_e < \sqrt{m_e/m_i}$, however, even for $\beta_e \lesssim 1$ it produces only small deviations from the full electromagnetic model and still works quite well.

3.4.5. High Beta Case

The high beta case is best fit by the parameters $R = 1.00$, $S = 0.407$, $x_{g1e} = -0.967\rho_i$, $x_{g2e} = -0.571\rho_i$, $x_{g1i} = -1.57\rho_i$, $x_{g2i} = -0.534\rho_i$, $n_0 = 0.461$ cm^{-3}, and $B_0 = 3.93$ nT. Temperature gradients, temperature anisotropy, and electromagnetic effects are all important for this case and are necessary to reproduce the density, magnetic fields, and temperatures. Figure 11 shows the plasma density and magnetic field for the MMS high beta case and the model, while Figure 12 shows the temperatures. The electron temperature gradient predicted by the theory is steeper than that of the data, though the temperature data for this case does not have a high enough resolution in x/ρ_i to state whether there is a discrepancy.

This case is interesting in that while there is a density gradient and temperature gradient for the electrons, they cancel out and result in no pressure gradient (and thus no diamagnetic drift). Because of the way the temperature gradient is modeled in section 3.3, it is not able to fully capture this feature. Use of a more

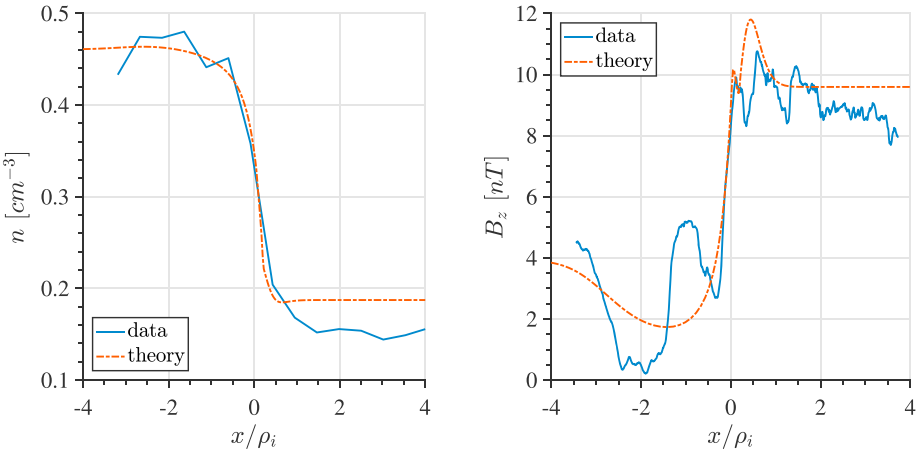

Figure 11. The plasma density (left) and magnetic field (right) for the high beta case from Magnetospheric Multiscale and the model that best fits these data.

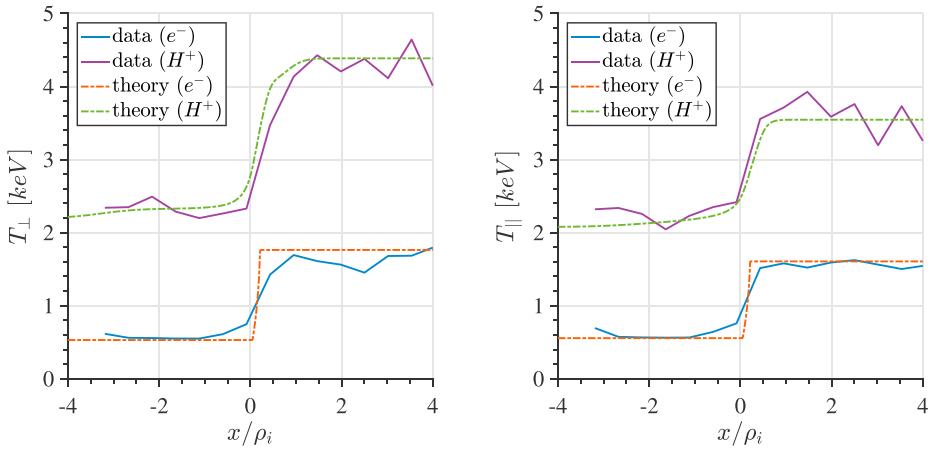

Figure 12. The perpendicular temperature (left) and parallel temperature (right) for the high beta case from Magnetospheric Multiscale and the model that best fits these data.

general temperature profile would likely result in a model that is not analytic. Allowing separate $x_{g1\alpha}$ and $x_{g2\alpha}$ parameters for the density and temperature profiles would be another solution, though in our experience this results in overfitting to the data. The associated temperatures are $\kappa T_{e0\perp,R} = 530$ eV, $\kappa T_{e0\perp,S} = 1,763$ eV, $\kappa T_{e0\parallel,R} = 556$ eV, $\kappa T_{e0\parallel,S} = 1,606$ eV, $\kappa T_{i0\perp,R} = 2,170$ eV, $\kappa T_{i0\perp,S} = 4,385$ eV, $\kappa T_{i0\parallel,R} = 2,078$ eV, and $\kappa T_{i0\parallel,S} = 3,545$ eV. This fit is more challenging due to the large fluctuations in the magnetic field.

4. Stability Analysis

The stability of a DF may be broadly grouped into three frequency domains depending on the wave time scale and nuances of the plasma distribution: (i) high frequency ($\omega \gg \omega_{LH}$, where $\omega_{LH} = \omega_{pi}/\sqrt{1+\omega_{pe}^2/\Omega_e^2}$ is the lower-hybrid frequency) in which the wave time scale is so fast that ions can hardly move on that time scale and consequently their contribution is just a passive charge neutralizing background, (ii) intermediate frequency ($\omega \sim \omega_{LH}$) in which the ion orbits can be treated as ballistic because their gyroperiod is much longer than the wave time scale making them effectively an unmagnetized species, and (iii) low frequency ($\omega \ll \omega_{LH}$) in which the ions can execute complete gyro motion over the wave time scale. The electron and ion plasma frequencies are denoted by $\omega_{p\alpha} = \sqrt{4\pi n_\alpha e^2/m_\alpha}$.

4.1. Dispersion Relation

For detailed stability analysis consider the maximum velocity shear region where $\Omega_e > dv_E/dx > \Omega_i$, which is located in the electron layer. Since $\rho_i > L > \rho_e$ in this region, where L is the scale size of the ambipolar electric field, the electrons sample the electric field over their complete gyro orbit and execute a complete $\vec{E}\times\vec{B}$ drift. But the ions sample the electric field only for a fraction of their gyro orbit resulting in a smaller gyro-averaged ion $\vec{E}\times\vec{B}$ drift compared to the electrons. This results in different flow profiles for the ions and the electrons as found in Figure 7. For a sufficiently small L the ions experience negligible electric field force and consequently their distribution function reduces to a Maxwellian. The fastest growing intermediate frequency ($\Omega_i < \omega < \Omega_e$) waves with $k_\perp\rho_i > 1 > k_\perp\rho_e$ have long parallel wavelength, that is, $k_\parallel \to 0$, for which Landau damping is negligible. For these fast growing ($Im(\omega) \geq \Omega_i$) waves the ion cyclotron harmonics may be integrated, which reduces the ion density fluctuation to that of an unmagnetized species (Ganguli et al., 1988a),

$$\tilde{n}_i(x) = \frac{1}{4\pi e}\frac{\omega_{pi}^2}{\omega^2}\left(k_y^2 - \frac{d^2}{dx^2}\right)\tilde{\phi}(x), \tag{15}$$

where $\tilde{\phi}(x)$ is the fluctuating wave potential and e is the electronic charge. Due to the strong spatial inhomogeneity in the $\hat{e}_x$ direction, the assumption of plane wave solutions in this direction is invalid and the normal Fourier transform is not useful. Consequently, the operator d/dx appears in equation (15), which will lead to a spatially localized wave packet in the $\hat{e}_x$ direction and an eigenvalue condition for the wave dispersion.

For electrons the weak shear limit can be applied because $\epsilon = \rho_e/L < 1$ and $\eta_e(x) = 1 + (dv_E/dx)/\Omega_e > 0$ (Ganguli et al., 1988b). In this limit the distribution function simplifies to

$$f_{0e} \simeq \frac{n_{0e}}{\sqrt{\eta_e(x)}(\pi v_{te}^2)^{3/2}} \exp\left(-\left(v_x^2 + (v_y - v_E(x))^2/\eta_e(x) + v_z^2\right)/v_{te}^2\right), \tag{16}$$

where $v_E(x) = \langle -cE_x(x)/B \rangle_g$ is the gyro-averaged $\vec{E} \times \vec{B}$ drift. Using this distribution function the first order electron density fluctuations are (Ganguli et al., 1988b)

$$\begin{aligned} \tilde{n}_e(x) = -\frac{\omega_{pe}^2}{4\pi v_{te}^2 e}\Bigg[-\sum_n \left(\frac{\omega_1 + \omega_{2e} - \omega_*}{\sqrt{2}|k_\parallel| v_e}\right) Z\left(\xi_n\right) \frac{d\Gamma_n(b_e)}{db} \rho_e^2 \frac{d^2}{dx^2} \\ +1 + \sum_n \left(\frac{\omega_1 + \omega_{2e} - \omega_*}{\sqrt{2}|k_\parallel| v_e}\right) Z\left(\xi_n\right) \Gamma_n(b_e)\Bigg] \tilde{\phi}(x), \end{aligned} \tag{17}$$

where terms of the order $\rho_e^4(d^4/dx^4) \sim \epsilon^4$ and higher are neglected. In the above, $b = (k_y\rho_e)^2$, $\Gamma_n(b) = \exp(-b)I_n(b)$, and $I_n(b)$ is the modified Bessel function. Also, $Z(\xi) = \sqrt{\pi}\int_{-\infty}^{\infty} dt \exp(-t^2)/(t-\xi)$ is the plasma dispersion function and $\xi_n = (\omega_1 - \omega_{2e} - n\Omega_e)/(\sqrt{2}|k_\parallel| v_{te})$. The transverse electric field is inhomogeneous and hence the $\vec{E} \times \vec{B}$ drift cannot be transformed away, which affects the physics by introducing new frequencies (i.e., time scales) into the system. The Doppler shifted frequency due to the electric field is $\omega_1 = \omega - k_y v_E(x)$, the frequency associated with the electric field curvature ($v_E'' = d^2v_E/dx^2$) is $\omega_{2e} = k_y v_E''(x)\rho_e^2/2$, and the diamagnetic drift frequency is $\omega_* = k_y \epsilon_{ne} \rho_e \Omega_e$, where $\epsilon_{ne} = \rho_e/L_n$, and $L_n = n_e/(dn_e/dx)$, is the scale size of the density gradient. For $\omega < \Omega_e$, only the $n = 0$ electron cyclotron harmonic is important in the electron density fluctuation. For perpendicular wavelengths long compared to the electron gyroradius ($1 > k_\perp \rho_e$) we can expand $\Gamma_0(b) \sim 1 - b$ by neglecting terms of the order of ϵ^4. We consider parallel wavelengths to be long to avoid Landau damping ($\xi_0 > 1$) so the Z function can be expanded for large argument and equation (17) simplifies to

$$\tilde{n}_e(x) = -\frac{\omega_{pe}^2}{4\pi\Omega_e^2 e}\left[-\frac{d^2}{dx^2} + \left\{k_y^2 - k_y\left(\frac{V_E''(x) - \Omega_e/L_n}{\omega - k_y v_E(x)}\right)\right\}\right]\tilde{\phi}(x). \tag{18}$$

Combining equations (15) and (18) with Poisson's equation gives the dispersion relation for the fastest growing intermediate frequency waves in DFs,

$$\left[\frac{d^2}{dx^2} - k_y^2 + \left(\frac{\omega_{pe}^2}{\omega_{pe}^2 + \Omega_e^2}\right)\left(\frac{\omega^2}{\omega^2 - \omega_{LH}^2}\right)\frac{k_y\left(v_E''(x) - \Omega_e/L_n\right)}{\omega - k_y v_E(x)}\right]\tilde{\phi}(x) = 0. \tag{19}$$

4.2. Dominant Modes

Equation (19) could have been derived by a fluid formalism, which implies that the dominant modes in the intermediate frequency range in a DF are nonresonant. If the electric field curvature is neglected (i.e., $v_E''(x) \to 0$) then the in local limit $d/dx \to ik_x$ and equation (19) reduces to the dispersion relation for the LHD instability (Krall & Liewer, 1971; Mikhailovskii & Tsypin, 1966). Growth of these modes depends upon the density gradient and hence their growth relaxes the density gradient. For a weak density gradient, that is, $\Omega_e/L_n \to 0$, equation (19) reduces to the eigenvalue condition for the electron-ion hybrid (EIH) instability where the free energy is obtained from the sheared electron flow through fast time averaging by the perturbations (Ganguli et al., 1988a). The growth of these waves relaxes the velocity shear. The relative strength of the two terms in the numerator of the last term in equation (19) determines the dominant waves in the intermediate frequency range that are generated in the DF.

From equation (19) it is clear that the intermediate frequency waves depend on a double resonance $\omega \simeq \omega_{LH} \simeq k_y v_E(x)$. The resonance with $k_y v_E(x)$ is particularly important because it can increase the electron Landau damping. Hence, the limit where Landau damping is eliminated and both the EIH and LHD instability growth are maximized is used to determine the most likely modes in a DF. The modified two stream instability (McBride et al., 1972), which is another intermediate frequency wave that requires $k_\parallel \neq 0$, is included in the model but its contribution is minimal because $k_\parallel \to 0$ where the growth rate of the intermediate frequency waves is largest.

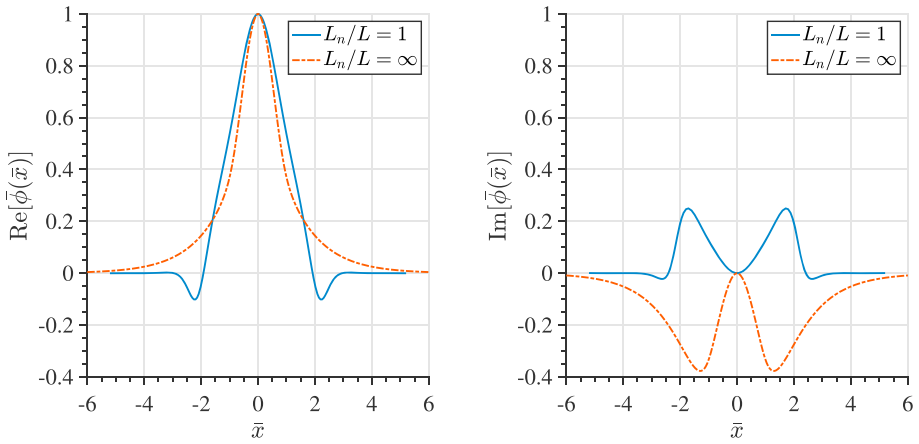

Figure 13. Eigenfunctions (real part on the left and imaginary part on the right) for $L_n/L = 1$ and $L_n/L = \infty$ and $\alpha = 1$ with $k_y L$ chosen to maximize the growth rate.

For our case of interest $\omega_{pe}^2 \gg \Omega_e^2$, so $\omega_{LH} \simeq \sqrt{\Omega_i \Omega_e}$ and the first factor in the third term of equation (19) is about one. We now put the eigenmode equation, equation (19), in dimensionless form,

$$\left[\frac{d^2}{d\bar{x}^2} - \bar{k}^2 + \left(\frac{\bar{\omega}^2}{\bar{\omega}^2 - 1^2}\right)\frac{\bar{k}\left(\alpha \bar{v}_E''(\bar{x}) - L/L_n\right)}{\bar{\omega}\sqrt{\mu} - \bar{k}\alpha \bar{v}_E(\bar{x})}\right]\bar{\phi}(x) = 0, \tag{20}$$

where $\bar{x} = x/L$, $\bar{\omega} = \omega/\omega_{LH}$, $\bar{k} = k_y L$, $\bar{v}_E(x) = v_E(x)/v_0$, $v_0 = E_0/B_0$, $\alpha = v_0/(L\Omega_e)$ is the shear parameter, and $\mu = m_e/m_i$,

Figure 13 shows two solutions to equation (20) (i.e., the real and imaginary parts of the eigenfunctions). Figure 14 is a plot of the linear growth rate and the real frequency obtained from solving the eigenvalue condition given in equation (20). The eigenfunctions and eigenvalues were found via a shooting method in which the large $\bar{x}$ solution goes to zero at infinity. In the region of interest the density profile can be approximated by $n(x) = n_0 \tanh(x/L_n)$ and the electron flow profile by $E(x) = E_0 \mathrm{sech}^2(x/L)$. In a fluid model $L/L_n = 1$ because the electric field is directly proportional to the density gradient for constant temperature. In the kinetic model, however, the electric field is due to ambipolar effects and is not proportional to the density gradient when L_n becomes comparable to or less than ρ_i, hence the scale size of the density gradient and the electric field are not identical. As the shear parameter is increased, implying higher compression, the growth rate increases. The real frequency is around the lower-hybrid frequency while Doppler shifting broadens the frequency spectrum. The bandwidth increases with shear parameter.

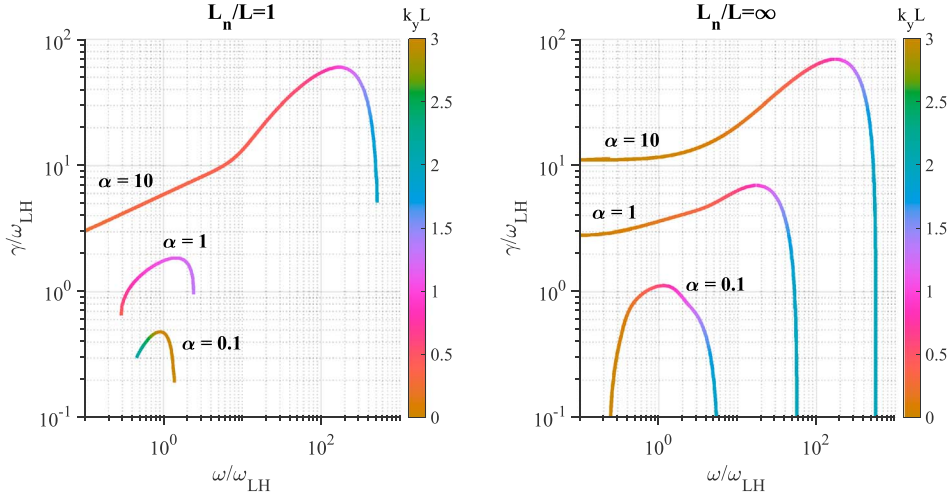

Figure 14. Linear growth rate as a function of real frequency, colored by associated k_y value. On the left is the fluid case, where the electric field balances the density gradient. On the right is the limit of the kinetic case.

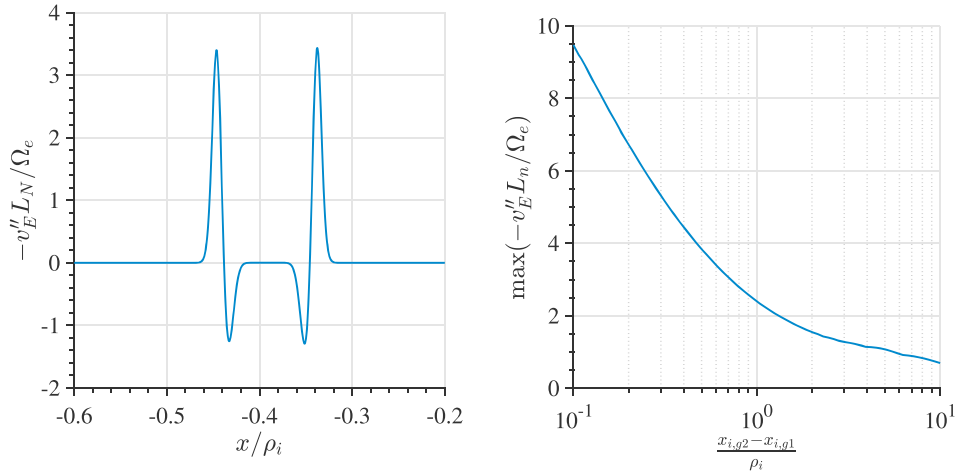

Figure 15. The ratio of the two driving terms in equation (19) as a function of x (left) and as a function of layer width (right).

In the two cases shown, the growth peaks for $k_y L \sim 1$. The wavelength is much longer than ρ_e since $L \gg \rho_e$. As L_n/L is reduced, the wavelengths become shorter and in the limit of uniform electric field ($L \to \infty$) it is well known that $k\rho_e \sim 1$ (Krall & Liewer, 1971). Note that these discrete eigenmodes in x are still continuously dependent on k_y. In section 5 we study the nonlinear evolution of this equilibrium condition and its observable signatures by PIC simulation and show that the spectral bandwidth becomes even broader nonlinearly as lower frequency waves are naturally triggered with increasing L. Since equation (20) contains both density and electric field gradients, an interesting question is which one of these is responsible for the waves?

Figure 15 compares the relative strength of the LHD and the EIH terms in equation (20). The left plot shows the ratio of these EIH to LHD terms for the low beta MMS case as a function of position (focused on the electron layer). It shows that even for weak compression, as in the case considered, the EIH term is three times as large as the LHD term. In the stronger compression high beta case (not shown), the EIH term is more than an order or magnitude larger. Figure 15 shows the maximum of the ratio of EIH/LHD terms as the compression is increased. The right plot shows the ratio of these terms as a function of layer width; this plot was made by using the same parameters as the low beta case and compressing and expanding the layer via choice of $x_{g1\alpha}$ and $x_{g2\alpha}$. Clearly, the EIH instability dominates over the LHD instability as long as the scale size of the density gradient is comparable to ion gyroradius or less, which is the typical condition prevailing in DFs.

We ignored the inhomogeneity in the magnetic field here for simplicity. In the region of interest around $x/\rho \approx -0.4$ the magnetic field gradient is too weak to make a difference. Stronger gradients result in a stronger EIH instability (Romero & Ganguli, 1994), but a weaker LHD instability (Davidson et al., 1977). In section 3 we found that for the high beta case, a gradient in the temperature also develops but in the opposite direction to the density gradient, which makes the pressure gradient (and hence the diamagnetic drift) weaker but reinforces the ambipolar effects resulting in enhanced sheared flows. This also favors the EIH instability over the LHD instability. Thus, in a typical DF configuration, the EIH mechanism will dominate wave generation and hence the nonlinear evolution, highlighting the importance of the ambipolar electric field.

In general, the self-consistent generation of an ambipolar electric field is unavoidable in warm plasmas with a density gradient of scale size comparable to or less than the ion gyroradius. This raises an interesting question: Does the classical "textbook variety" of the LHD instability exist at all? While a transverse electric field has long been used to balance the equilibrium density gradient in LHD wave analyses, it was usually considered to be uniform (Krall & Liewer, 1971). In numerical simulations of the LHD waves, however, the electric field must be sheared as discussed by Y. J. Chen et al. (1983), but its role as an independent source of free energy for the intermediate frequency waves had not been realized until 1990s (Romero et al., 1992; Romero & Ganguli, 1993) because the existence of the EIH modes (Ganguli et al., 1988a) was unknown. The

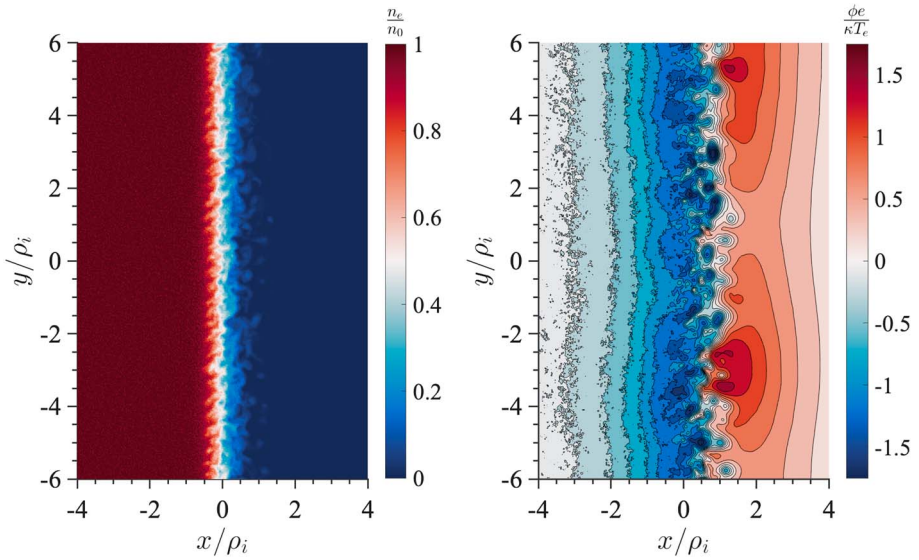

Figure 16. Plasma density, n, (left) and electrostatic potential, ϕ, (right) at $t \approx 28/\omega_{LH}$. Waves in the $\hat{e}_y$ direction and vortices are both visible.

dominance of the EIH over LHD wave becomes further evident in the nonlinear analysis of DF stability in the following section.

5. Simulation of Nonlinear Evolution

Now we use a PIC simulation to study the nonlinear evolution of the fluctuations described in section 4. The code is the same as the one in section 3.4, except now the simulation is two dimensional in the plane perpendicular to the magnetic field. Because the conditions for growth of intermediate frequency waves are met in the electron layer and to keep the simulation tractable, we limit the simulation to this layer (similar to Romero & Ganguli, 1993). This simulation is meant to study the generation, growth, and saturation of the waves in order to understand the spectral signature for comparison with observation. A more detailed study of the nonlinear evolution in three dimensions in order to fully analyze the dynamics of the vortices formed and nonlinear scatterings is the subject of a future paper. The plasma frequency to cyclotron frequency ratio is $\omega_{pe}/\Omega_e = 3.59$, beta is $\beta_e = 0.035$, the mass ratio is $m_e/m_i = 1/400$, and the driving ambipolar field is given by $E_0/B_0 = 0.32v_{te}$. The simulation time is $175/\omega_{LH}$, the domain is $21\rho_i$ by $21\rho_i$ (1,200 by 1,200 cells), boundaries are periodic in all directions (two mirrored layers are employed as in section 3.4.2), and there are 537 million particles.

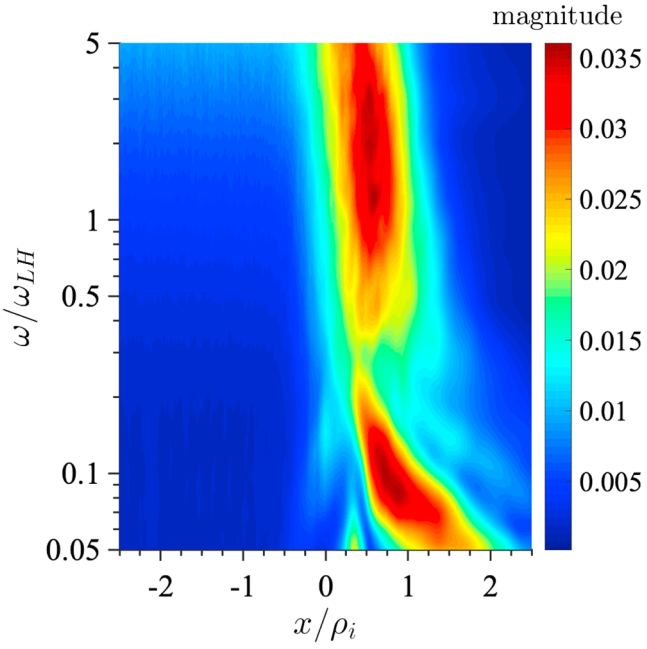

Figure 17. Wavelet spectrum of the electric field as a function of position near $t \approx 28/\omega_{LH}$. The density gradient is steepest near $x/\rho_e = 0$.

Figure 16 shows a snapshot of the plasma density and electrostatic potential from the simulation at $t \approx 28/\omega_{LH}$. These images depict only a part of the simulation domain in order to make features more visible. Kinking is seen in the density. Vortices are formed on the lower density (right) side of the layer as well; these are visible in the potential (e.g., one vortex is located at $(x/\rho_i, y/\rho_i) \approx (1, -1.5)$). Wave activity in the $\vec{e}_y$ direction with $k_y L \sim 1$ is apparent in both the density and the potential. The growth rate of the field energy in the simulation is consistent with the growth rate found by solving equation (20). The mass ratio of the simulation is artificially low; a physical mass ratio would enhance the ambipolar electric field and further drive these waves.

Figure 17 is a wavelet spectrum as a function of x position; the layer is centered near $x/\rho_i = 0$. It is meant to mimic what a satellite would see if it were flying through the simulated layer, similar to the MMS

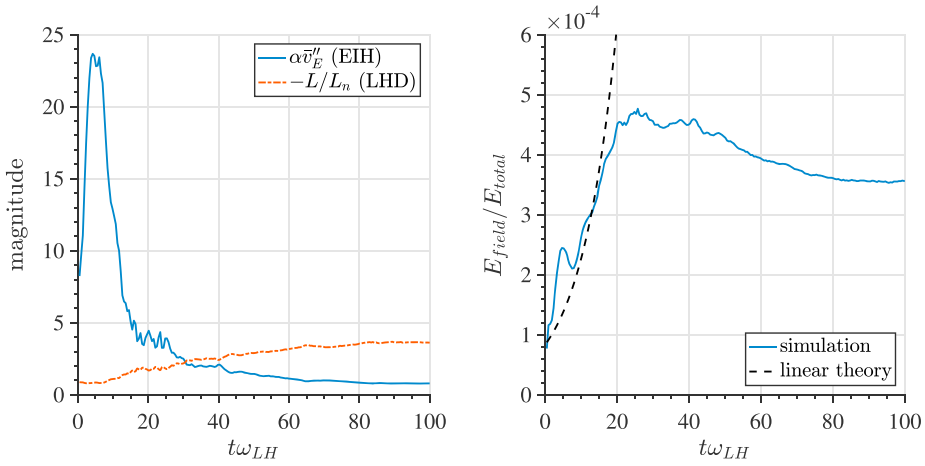

Figure 18. The driving terms for the EIH instability and LHD instability (left) and the field energy fraction (right) in the simulation as a function of time. EIH = electron-ion hybrid; LHD = lower-hybrid drift.

measurements in Figures 1g and 2g. There are broadband waves spread around and above the lower-hybrid frequency, as expected from equation (20) and Figure 14. The lower frequency power $\omega/\omega_{LH} \approx 0.1$ is consistent with vortices being generated and propagating away from the layer. In laboratory experiments, lower frequency waves ($\omega < \omega_{LH}$) are also seen with DF-like conditions (DuBois et al., 2014).

As time passes in the simulation, the density gradient slightly relaxes while the electron flow in the $\vec{e}_y$ direction and accompanying electric field $\vec{e}_x$ direction significantly relax, indicating the dominance of shear-driven instability (EIH) over the density gradient-driven instability (LHD). Figure 18 shows the ratio of these two terms (as seen in equation (20)) and the field energy as a function of simulation time. Instability growth and wave emission occurs before $t = 20/\omega_{LH}$. The dotted black line is the theoretical linear growth predicted by equation (20). During the growth phase, the EIH term (and thus the velocity shear) is clearly falling, suggesting that the shear is the source of free energy for the waves. The simulation reaches a saturated state at $t \approx 20/\omega_{LH}$.

6. Concluding Remarks

We present a kinetic framework to study the small-scale features of DFs, which are compressed plasma layers with density gradients in the normal direction with characteristic scale sizes comparable to an ion gyroradius. Large-scale (mesoscale or global scale) simulations that can resolve small gyro scale features must be kinetic, have sufficient mass ratios to generate the ambipolar electric field, and cannot use implicit methods to skip over this essential boundary layer physics. Consequently, the gyro scale phenomena such as ambipolar effects that are important to the dissipation mechanisms have been previously ignored. The kinetic model we present highlights the importance of the ambipolar electric field across the magnetic field that must naturally arise to support the gyro scale equilibrium structures as observed. The presence of the ambipolar field leads to a distinctive non-Maxwellian plasma distribution, which includes sheared flows in the DFs. In order to show this equilibrium model is grounded in reality, we have fit it to two MMS DF events; further work will contain more detailed comparisons to particular events as well as a statistical analysis of many measured events.

Analysis of the linear stability of compressed plasmas in a typical DF using the distribution indicates that waves in a broad frequency spectrum can be generated by the velocity shear (or equivalently, the ambipolar electric field across the magnetic field), which arises self consistently in response to the global compression. To investigate the nonlinear features we have used a PIC simulation to study the evolution of the plasma distribution and the resulting self-consistent waves to compare with observations. We find that the sheared electron flow generates a broadband spectral signature in the lower-hybrid frequency range. Their nonlinear evolution relaxes the velocity shear, which helps to reach a steady or saturated state that is found to be consistent with observations. The frequency and wave vectors are proportional to the velocity shear. In the nonlinear stage vortices are observed to form, which can be seen as coherent electron depletion regions with scale sizes comparable to the sheared flow scale size. During the relaxation process lower frequency waves

can be progressively generated, which leads to nonlinear broadening of the spectrum. This is in addition to the spectral broadening of the linear spectrum due to Doppler shifting.

While we discuss how large-scale physics (i.e., global compression) leads to small-scale equilibrium features in a DF, which results in broadband emissions around the lower-hybrid frequency, an important consequence of the generated waves that we have not explored in this paper is their contribution to larger-scale physics. For example, viscosity and resistivity generated by these microscale waves can influence the mesoscale dynamics of the DFs. Romero and Ganguli (1993) investigated the generation of viscosity and resistivity from simulations and provided expressions relating the magnitude of these quantities to the wave amplitude. Therefore, the effects of the kinetic scale physics could potentially be included in larger-scale fluid models for a more holistic representation of the physics. The possibility of such cross-scale coupling will be explored in the future. Another consequence to be explored in a future work is how effectively can the shear-generated waves (through finite parallel wavelengths or stochastic wave heating) contribute to particle energization.

In our previous work (Ganguli et al., 2018) we showed that when the larger-scale dipolar magnetic geometry is considered an electric field is also generated along the magnetic field lines, due to global compression. This parallel electric field can accelerate the nonthermal particles into parallel beams. These parallel beams can also be the source of free energy for waves and add to the broadband spectrum. Detailed analysis of the physics along the magnetic field has yet to be addressed.

In the future we also plan to investigate the kinetic physics of the DF and their connection to larger-scale physics through laboratory experiments. In general, it is not easy to scale space plasma phenomena in a finite size laboratory device. However, due to the gyro scale dimension of the DFs, they are especially amenable to scaled experiments in the laboratory. These experiments are ideal for detailed characterization of the phenomenon by producing an electric field localized over a distance on the order of the ion gyroradius transverse to the magnetic field as observed in a DF. A number of controlled laboratory experiments (Amatucci et al., 2003; DuBois et al., 2014; Enloe et al., 2017) demonstrated the generation of waves in the lower-hybrid frequency range when DF-like plasma conditions were generated in the laboratory by introducing a localized electric field transverse to the magnetic field. Laboratory experiments allowed detailed characterization of the wave spectrum and their nonlinear properties, which led to validation of that theory.

Acknowledgments
This work was supported by Naval Research Laboratory Base Program and NASA grant NNH17AE70I. Simulations were performed on the Centennial supercomputer at Army Research Laboratory. All MMS data used in this work are publicly available and can be found online (https://lasp.colorado.edu/mms/sdc/public/).

References

Amatucci, W. E., Ganguli, G., Walker, D. N., Gatling, G., Balkey, M., & McCulloch, T. (2003). Laboratory investigation of boundary layer processes due to strong spatial inhomogeneity. *Physics of Plasmas*, *10*(5), 1963–1970. https://doi.org/10.1063/1.1562631

Birdsall, C. K., & Langdon, A. B. (2004). *Plasma physics via computer simulation*. New York: CRC Press.

Birn, J., & Hesse, M. (2014). Forced reconnection in the near magnetotail: Onset and energy conversion in PIC and MHD simulations. *Journal of Geophysical Research: Space Physics*, *119*, 290–309. https://doi.org/10.1002/2013JA019354

Birn, J., Nakamura, R., Panov, E. V., & Hesse, M. (2011). Bursty bulk flows and dipolarization in MHD simulations of magnetotail reconnection. *Journal of Geophysical Research*, *116*, A01210. https://doi.org/10.1029/2010JA016083

Burch, J. L., Moore, T. E., Torbert, R. B., & Giles, B. L. (2016). Magnetospheric multiscale overview and science objectives. *Space Science Reviews*, *199*(1), 5–21.

Chaston, C. C., Bonnell, J. W., Wygant, J. R., Mozer, F., Bale, S. D., Kersten, K., et al. (2014). Observations of kinetic scale field line resonances. *Geophysical Research Letters*, *41*, 209–215. https://doi.org/10.1002/2013GL058507

Chen, Y. J., Nevins, W. M., & Birdsall, C. K. (1983). Stabilization of lower-hybrid drift instability by resonant electrons. *Physics of Fluids*, *26*, 2501–2508.

Chen, C. X., & Wolf, R. A. (1993). Interpretation of high-speed flows in the plasma sheet. *Journal of Geophysical Research*, *98*(A12), 21,409–21,419.

Davidson, R. C., Gladd, N. T., Wu, C. S., & Huba, J. D. (1977). Effects off inite plasma beta on the lower hybrid drift instability. *The Physics of Fluids*, *20*(2), 301–310. https://doi.org/10.1063/1.861867

DuBois, A. M., Thomas, E., Amatucci, W. E., & Ganguli, G. (2014). Experimental characterization of broadband electrostatic noise due to plasma compression. *Journal of Geophysical Research: Space Physics*, *119*, 5624–5637. https://doi.org/10.1002/2014JA020198

Enloe, C. L., Tejero, E. M., Crabtree, C., Ganguli, G., & Amatucci, W. E. (2017). Electromagnetic fluctuations in the intermediate frequency range originating from a plasma boundary layer. *Physics of Plasmas*, *24*, 052107. https://doi.org/10.1063/1.4981923

Ganguli, G., Crabtree, C., Fletcher, A. C., Tejero, E., Malaspina, D., & Cohen, I. (2018). Kinetic equilibrium of dipolarization fronts. *Scientific Reports*, *8*(1), 17186.

Ganguli, G., Lee, Y. C., & Palmadesso, P. J. (1988a). Electron–ion hybrid mode due to transverse velocity shear. *Physics of Fluids*, *31*(10), 2753–2756.

Ganguli, G., Lee, Y. C., & Palmadesso, P. J. (1988b). Kinetic theory for electrostatic waves due to transverse velocity shears. *Physics of Fluids*, *31*(4), 823–838.

Gkioulidou, M., Ohtani, S., Mitchell, D. G., Ukhorskiy, A. Y., Reeves, G. D., Turner, D. L., et al. (2015). Spatial structure and temporal evolution of energetic particle injections in the inner magnetosphere during the 14 July 2013 substorm event. *Journal of Geophysical Research: Space Physics*, *120*, 1924–1938. https://doi.org/10.1002/2014JA020872

Gkioulidou, M., Ukhorskiy, A. Y., Mitchell, D. G., Sotirelis, T., Mauk, B. H., & Lanzerotti, L. J. (2014). The role of small-scale ion injections in the buildup of Earth's ring current pressure: Van Allen Probes observations of the 17 March 2013 storm. *Journal of Geophysical Research: Space Physics*, *119*, 7327–7342. https://doi.org/10.1002/2014JA020096

He, Y., Sun, Y., Liu, J., & Qin, H. (2015). Volume-preserving algorithms for charged particle dynamics. *Journal of Computational Physics*, *281*, 135–147.

Hwang, K. J., Goldstein, M. L., F Viñas, A., Schriver, D., & Ashour-Abdalla, M. (2014). Wave-particle interactions during a dipolarization front event. *Journal of Geophysical Research: Space Physics*, *119*, 2484–2493. https://doi.org/10.1002/2013JA019259

Krall, N. A., & Liewer, P. C. (1971). Low-frequency instabilities in magnetic pulses. *Physical Review A*, *4*, 2094–2103. https://doi.org/10.1103/PhysRevA.4.2094

Liu, J., Angelopoulos, V., Zhang, X.-J., Turner, D. L., Gabrielse, C., Runov, A., et al. (2016). Dipolarizing flux bundles in the cis-geosynchronous magnetosphere: Relationship between electric fields and energetic particle injections. *Journal of Geophysical Research: Space Physics*, *121*, 1362–1376. https://doi.org/10.1002/2015JA021691

Liu, C. M., Fu, H. S., Vaivads, A., Khotyaintsev, Y. V., Gershman, D. J., Hwang, K. J., et al. (2018). Electron jet detected by MMS at dipolarization front. *Geophysical Research Letters*, *45*, 556–564. https://doi.org/10.1002/2017GL076509

Malaspina, D. M., Andersson, L., Ergun, R. E., Wygant, J. R., Bonnell, J. W., Kletzing, C., et al. (2014). Nonlinear electric field structures in the inner magnetosphere. *Geophysical Research Letters*, *41*, 5693–5701. https://doi.org/10.1002/2014GL061109

Malaspina, D. M., Wygant, J. R., Ergun, R. E., Reeves, G. D., Skoug, R. M., & Larsen, B. A. (2015). Electric field structures and waves at plasma boundaries in the inner magnetosphere. *Journal of Geophysical Research: Space Physics*, *120*, 4246–4263. https://doi.org/10.1002/2015JA021137

Mauk, B. H., Blake, J. B., Baker, D. N., Clemmons, J. H., Reeves, G. D., Spence, H. E., et al. (2016). The energetic particle detector (EPD) investigation and the energetic ion spectrometer (EIS) for the magnetospheric multiscale (MMS) mission. *Space Science Reviews*, *199*(1), 471–514.

McBride, J. B., Ott, E., Boris, J. P., & Orens, J. H. (1972). Theory and simulation of turbulent heating by the modified two stream instability. *The Physics of Fluids*, *15*(12), 2367–2383. https://doi.org/10.1063/1.1693881

Mikhailovskii, A. B., & Tsypin, V. S. (1966). High-frequency instability of a plasma in a radial electric and longitudinal magnetic field. *Journal of Experimental and Theoretical Physics Letters*, *3*, 158.

Nicholson, D. R. (1983). *Introduction to plasma theory*. New York: John Wiley and Sons.

Nosé, M., Koshiishi, H., Matsumoto, H., son Brandt, P. C., Keika, K., Koga, K., et al. (2010). Magnetic field dipolarization in the deep inner magnetosphere and its role in development of O+-rich ring current. *Journal of Geophysical Research*, *115*, A00J03. https://doi.org/10.1029/2010JA015321

Parks, G. K., Lin, C. S., Anderson, K. A., Lin, R. P., & Reme, H. (1979). ISEE 1 and 2 particle observations of outer plasma sheet boundary. *Journal of Geophysical Research*, *84*(A11), 6471–6476. https://doi.org/10.1029/JA084iA11p06471%

Pollock, C., Moore, T., Jacques, A., Burch, J., Gliese, U., Saito, Y., et al. (2016). Fast plasma investigation for magnetospheric multiscale. *Space Science Reviews*, *199*(1-4), 331–406. https://doi.org/10.1007/s11214-016-0245-4

Reeves, G. D., Henderson, M. G., McLachlan, P. S., Belian, R. D., Friedel, R. W., & Korth, A. (1996). Radial propagation of substorm injections, in International Conference on Substorms. In *Proceedings of the 3rd International Conference*, *389*, pp. 579.

Romero, H., & Ganguli, G. (1993). Nonlinear evolution of a strongly sheared cross-field plasma flow. *Physics of Fluids B: Plasma Physics (1989-1993)*, *5*(9), 3163–3181. https://doi.org/10.1063/1.860653

Romero, H., & Ganguli, G. (1994). Relaxation of the stressed plasma sheet boundary layer. *Geophysical Research Letters*, *21*(8), 645–648. https://doi.org/10.1029/93GL03385

Romero, H., Ganguli, G., Lee, Y. C., & Palmadesso, P. J. (1992). Electron-ion hybrid instabilities driven by velocity shear in a magnetized plasma. *Physics of Fluids B*, *4*, 1708–1723.

Runov, A., Angelopoulos, V., Sitnov, M. I., Sergeev, V. A., Bonnell, J., McFadden, J. P., et al. (2009). THEMIS observations of an earthward-propagating dipolarization front. *Geophysical Research Letters*, *36*, L14106. https://doi.org/10.1029/2009GL038980

Russell, C. T., Anderson, B. J., Baumjohann, W., Bromund, K. R., Dearborn, D., Fischer, D., et al. (2016). The magnetospheric multiscale magnetometers. *Space Science Reviews*, *199*(1), 189–256.

Sergeev, V. A., Angelopoulos, V., Gosling, J. T., Cattell, C. A., & Russell, C. T. (1996). Detection of localized, plasma-depleted flux tubes or bubbles in the midtail plasma sheet. *Journal of Geophysical Research*, *101*(A5), 10,817–10,826.

Sitnov, M. I., Merkin, V. G., Swisdak, M., Motoba, T., Buzulukova, N., Moore, T. E., et al. (2014). Magnetic reconnection, buoyancy, and flapping motions in magnetotail explosions. *Journal of Geophysical Research: Space Physics*, *119*, 7151–7168. https://doi.org/10.1002/2014JA020205

Sitnov, M. I., Swisdak, M., & Divin, A. V. (2009). Dipolarization fronts as a signature of transient reconnection in the magnetotail. *Journal of Geophysical Research*, *114*, A04202. https://doi.org/10.1029/2008JA013980

Sorathia, K. A., Ukhorskiy, A. Y., Merkin, V. G., Fennell, J. F., & Claudepierre, S. G. (2018). Modeling the depletion and recovery of the outer radiation belt during a geomagnetic storm: Combined MHD and test particle simulations. *Journal of Geophysical Research: Space Physics*, *123*, 5590–5609. https://doi.org/10.1029/2018JA025506

Sutmann, G. (2007). Compact finite difference schemes of sixth order for the Helmholtz equation. *Journal of Computational and Applied Mathematics*, *203*(1), 15–31.

Torbert, R. B., Russell, C. T., Magnes, W., Ergun, R. E., Lindqvist, P. A., Le Contel, O., et al. (2016). The FIELDS instrument suite on MMS: Scientific objectives, measurements, and data products. *Space Science Reviews*, *199*(1), 105–135.

Ukhorskiy, A. Y., Sitnov, M. I., Merkin, V. G., Gkioulidou, M., & Mitchell, D. G. (2017). Ion acceleration at dipolarization fronts in the inner magnetosphere. *Journal of Geophysical Research: Space Physics*, *122*, 3040–3054. https://doi.org/10.1002/2016JA023304

Wan, W., & Lapenta, G. (2008). Evolutions of non-steady-state magnetic reconnection. *Physics of Plasmas*, *15*(10), 102302.

Zhou, M., Ashour-Abdalla, M., Deng, X., Schriver, D., El-Alaoui, M., & Pang, Y. (2009). THEMIS observation of multiple dipolarization fronts and associated wave characteristics in the near-Earth magnetotail. *Geophysical Research Letters*, *36*, L20107. https://doi.org/10.1029/2009GL040663